3D geomechanical modeling of induced seismic slips considering realistic reservoir geometry with intersecting faults

Jingming Ruan[1], Ranajit Ghose[1], Wim A. Mulder[1,2]

[1]Delft University of Technology, the Netherlands
[2]Shell Global Solutions International B.V., the Netherlands

Key Points:

- The intersection angle between two normal faults affects the incremental stress field in a uniformly depleted reservoir
- The intersection angle affects the pattern of rupture propagation and the location of maximum slip during the induced seismicity
- The triggering depletion value and the amplitude of maximum slip for the seismic event are less affected by the fault intersection angle

Corresponding author: Jingming Ruan, `j.ruan@tudelft.nl`

Abstract

Geomechanical simulations of induced seismicity generally involve a simple reservoir geometry in terms of reservoir structure and fault distribution. Because the depletion of the reservoir controls the incremental stress field, the geometry of the reservoir has a substantial influence on the occurrence of induced earthquakes. We develop geomechanical models based on a realistic geological model of the reservoir in the Groningen gas field. The model captures the main characteristics of the reservoir structures in the Zeerijp region. Through quasi-static and dynamic simulations, we observe that a smaller intersection angle between the two normal faults in the Zeerijp region causes an increase in the incremental Coulomb stress at the lower reservoir juxtaposition adjacent to the intersection. As a result, this intersection angle strongly affects the location of the initial seismic slip, the rupture pattern, and the location of the maximum slip. Our simulation produces an earthquake of magnitude M_W 3.0, due to fault reactivation occurring at a reservoir depletion value of 26 MPa. These values are similar to those for the Zeerijp 2018 earthquake of M_L 3.4. The location of the simulated rupture is close to the inverted hypocenter location for the 2018 earthquake. Our results suggest that it is crucial to incorporate realistic reservoir structures when simulating induced seismicity in a specific region.

Plain Language Summary

Human activities, for example, underground gas extraction, can cause earthquakes that can damage the region. Faults in the reservoir are generally considered to be the host of strong earthquakes in the region. There are many factors affecting the timing and the magnitude of earthquakes, making it very difficult to predict or evaluate the possibility of having an earthquake in a specific period. In our research, we studied how gas extraction activities can cause earthquakes. By simulating earthquakes using realistic models of the reservoir in the Groningen gas field, especially in the Zeerijp region, we found that the intersection angle between two intersecting faults affects the resulting stress field on the faults in the reservoir from gas extraction. The affected stress field alternates the rupture propagation at the fault and the hypocenter of the earthquake. Our simulations showed an earthquake similar to the one in Zeerijp in 2018, with a magnitude of 3.4. This study highlights the importance of considering the actual reservoir shape when studying induced earthquakes, which can help predict and manage seismic events related to gas extraction more effectively.

1 Introduction

Earthquakes are occasionally caused by man-made activities, such as fluid extraction from or injection into the subsurface, inducing changes in the reservoir properties including changes in pore pressure that cause various mechanical responses in the reservoir and its surroundings. Production activities in a region with preexisting faults can reactivate those faults and generate earthquakes. There are various physical processes behind induced seismicity. In Groningen, the Netherlands, gas production is considered to be the main cause. There are numerous studies involving laboratory experiments on the frictional behavior of faults (Hunfeld et al., 2017) and numerical modeling based on geomechanics (Van Wees et al., 2017; DeDontney & Lele, 2018; Van den Bogert, 2018; Buijze et al., 2019), which try to explain the physical processes behind the induced seismicity in the Groningen region.

Kühn et al. (2022) reviewed several source models, including statistical and physical models, in order to investigate the cause of induced seismicity in Groningen. Geomechanical simulation is widely used to investigate the physical process behind induced seismicity. The pore-pressure variation in the reservoir induces poroelastic stress which, according to the Mohr-Coulomb theory, promotes the failure of the fractures in the reservoir. Apart from the poroelastic stress, the differential compaction due to faults with

non-zero offset can concentrate the incremental stresses caused by reservoir depletion, including shear stress and normal stress. This effect has been observed in numerical modeling by Van den Bogert (2018) and Buijze et al. (2019). Jansen and Meulenbroek (2022) derived an analytical description for a homogeneous medium.

In general, a simple 2-D or 3-D geometry has been used in most earlier geomechanical simulations of induced earthquakes in Groningen. These simulations essentially consider a horizontally-layered model with zero- or non-zero-offset faults. The effect of more realistic reservoir geometry on the generated induced earthquakes has been mostly ignored. One of the main features of the reservoir geometry is the fault system. Since faults, in general, occur as parts of a fault system, the reservoir is split by the fault system into multiple compartments, with a fault offset in the reservoir interval. Most earlier modeling studies on incremental stress fields in a depleted reservoir consider only reservoir compartments formed by a single fault with a non-zero offset. Such simple geometrical assumptions neglect the effect of fault intersection and the distribution of reservoir compartments. Maerten et al. (1999) numerically computed the irregular slip distributions caused by the interaction between the intersecting faults. The results were confirmed by seismic surveys and sandbox experiments.

In this research, our goal was to gain insights into the relationship between fault intersection and the induced seismicity caused by reservoir depletion. Through geomechanical simulations on models with different intersection angles from two normal faults, we found that the angle of the resulting horst structure strongly affects the incremental stress field in the reservoir juxtaposition, and thereby affects also the induced seismic event, including the hypocenter, the rupture pattern. In comparison, its effect on the triggering depletion value and the maximum slip during a seismic event is limited.

This article is structured as follows. In Section 2 we will first introduce the workflow of our simulation of induced earthquakes and the governing equations in each stage. We will discuss the methods involved in model construction, such as mesh design (geometry), discretization, boundary conditions, and assignment of material/fault parameters. In Section 3, we will present the 2-D models used for benchmarking, with and without an offset at the reservoir. Next, in Section 4, we will illustrate the design of 3-D models. The results on three-block models considering different intersection angles between the two normal faults will be presented, primarily focusing on the induced stress field and the dynamic rupture patterns. In Section 5, we will show how we constructed a realistic 3-D model of the reservoir geometry in the Zeerijp region located in the Groningen province. The relevance of this model to simulate the 2018 M_L 3.4 Zeerijp earthquake will be discussed. Section 6 summarizes our findings.

2 Numerical simulation and model setup

To simulate the induced seismicity in the Groningen gas field, we consider the poroelastic problem of reservoir compaction due to gas extraction, where the strain field is coupled with the pore-pressure field. For numerical simulations, the finite-element method (FEM) is widely used for stress and strain analyses in continuum mechanics. We have adapted the open-source finite-element code `Defmod` developed by Meng (2017) to simulate the strain, stress, and the resulting rupture at a uniformly depleted reservoir. `Defmod` is capable of both quasi-static and dynamic simulations, which are combined to simulate the evolution of the induced seismicity. To investigate the effect of fault intersection and the distribution of the reservoir compartments on induced seismicity, we develop a set of 3-D models with two intersecting normal faults and another realistic 3-D model based on the Petrel geological model of the Groningen gas field (NAM, 2020), concentrating on the Zeerijp reservoir geometry.

2.1 Quasi-static loading

Gas extraction and the resulting pore-pressure change in a reservoir can be regarded as a gradual loading process. Therefore, during this slow process, the inertial force can be neglected. We apply quasi-static simulation to simulate the incremental stress field at a depleted reservoir. The time step is set in the order of days, months or years for each iteration of the quasi-static simulation.

For quasi-static loading, `Defmod` considers a linear constitutive law applied to small-strain problems, and solves the (quasi-)static state of the linear system

$$\begin{aligned} \mathbf{K}_n \mathbf{U}_n &= \mathbf{F}_n \text{ (absolute)}, \\ \mathbf{K}_n \Delta\mathbf{U}_n &= \Delta\mathbf{F}_n \text{ (incremental)}, \end{aligned} \tag{1}$$

where $\mathbf{K}$ is the system stiffness matrix, $\mathbf{U}$ the solution vector, and $\mathbf{F}$ the nodal force including a fluid source. The subscript n is the time index. When solving a poroelastic problem such as reservoir depletion, the solution $\Delta\mathbf{U}_n$ includes the nodal displacement and pressure, where $\Delta\mathbf{U}_n = [\Delta\mathbf{u}_n, \Delta\mathbf{p}_n]^{\mathrm{T}}$.

When solving the poroelastic problem, the stiffness matrix $\mathbf{K}_n$ and the right-hand-side vector $\mathbf{F}_n$ are

$$\mathbf{K}_n = \begin{bmatrix} \mathbf{K}_e & \mathbf{H} \\ -\mathbf{H}^{\mathrm{T}} & \Delta t\, \mathbf{K}_c + \mathbf{S}_p \end{bmatrix}, \quad \mathbf{F}_n = \begin{bmatrix} \Delta\mathbf{f}_n \\ \mathbf{q}_n - \Delta t\, \mathbf{K}_c \mathbf{p}_{n-1} \end{bmatrix}, \tag{2}$$

with elastic stiffness matrix $\mathbf{K}_e$ depending on the elastic constants of the solid. The fluid stiffness matrix $\mathbf{K}_c$ depends on the fluid-flow conductivity. The coupling matrix $\mathbf{H}$ depends on Biot's coefficient and is responsible for coupling the displacement and the pressure fields. The storage matrix $\mathbf{S}_p$ depends on the compressibility and porosity of the solid, as well as on the compressibility of the fluid. The solution of the system provides an equilibrium between the displacement and the pressure fields.

In this study, we consider a highly permeable reservoir located in a relatively small part of the area of interest. Therefore, during the simulation, we could assume uniform depletion in the reservoir and keep the pore pressure outside the reservoir the same as the initial hydrostatic pressure. To this end, unlike Meng (2017), we manually define $\Delta\mathbf{p}_n$ in equation (2), multiply it with the stiffness matrix $\mathbf{K}_n$, and move the result to the right-hand-side function $\Delta\mathbf{F}_n$. Then, the solution of the system provides the displacement field $\Delta\mathbf{u}_n$ caused by the assumed uniform depletion or by any manually assigned $\Delta\mathbf{p}_n$. In our case, the governing equation (2) becomes

$$\mathbf{K}_e \Delta\mathbf{u}_n = \Delta\mathbf{f}_n - \mathbf{H}\Delta\mathbf{p}_n. \tag{3}$$

With this assumption, the quasi-static time step $\Delta\mathbf{t}$ does not affect the simulation, as $\Delta\mathbf{t}$ as well as the terms for fluid flow are no longer present in the governing equation. The unknown $\Delta\mathbf{u}_n$ is now related to the imposed depletion $\Delta\mathbf{p}_n$.

In `Defmod`, the fault constraints are implemented via a Lagrange Multiplier (LM) capping method. For a model containing a fault, each node except the edge nodes of the fault is split into a node pair sharing the same coordinates. Then, the node pairs are assigned separately to the elements that contained the same fault node before the split, based on which side the elements are located—either the positive side or the negative side of the fault in relation to its normal vector. These constraints limit the displacement and the pressure of the node pairs. As an example, Eq. (4) illustrates a locked and permeable fault by constraining tangential and normal displacements as well as the pres-

sure on the split fault nodes:

$$\begin{bmatrix} n_x & n_z & 0 & -n_x & -n_z & 0 \\ t_x & t_z & 0 & -t_x & -t_z & 0 \\ 0 & 0 & 1 & 0 & 0 & -1 \end{bmatrix} \begin{bmatrix} u_x^{(+)} \\ u_z^{(+)} \\ p^{(+)} \\ u_x^{(-)} \\ u_z^{(-)} \\ p^{(-)} \end{bmatrix} = 0. \tag{4}$$

Here, $u_x^{(+)}$ and $u_x^{(-)}$ are the x-axis displacements of the separated node pairs from the positive side and the negative side of the fault, respectively, depending on the normal vector $\mathbf{n}$ of the fault. The nodal pressures are $p^{(+)}$ and $p^{(-)}$, and $\mathbf{t}$ is the tangent vector of the fault. By combining the governing equation and the constraint equation, the system becomes

$$\begin{bmatrix} \mathbf{K} & \mathbf{G}^{\mathrm{T}} \\ \mathbf{G} & \mathbf{0} \end{bmatrix} \begin{bmatrix} \Delta \mathbf{U}_n \\ \boldsymbol{\lambda}_n \end{bmatrix} = \begin{bmatrix} \Delta \mathbf{f}_n \\ \mathbf{I}_n \end{bmatrix}, \tag{5}$$

where $\mathbf{G}$ is the constraint matrix, and $\boldsymbol{\lambda}_n$, the vector with Lagrange multipliers, contains the nodal forces and the pressure sources needed to satisfy the constraints, and thus becomes a proxy for the stress field of a fault. At each quasi-static time step, the stress field is calculated. Then, depending on the applied friction law, the state of the fault is evaluated. In this study, we apply the slip-weakening friction law. If the shear stress on a fault exceeds the fault strength, we switch to the dynamic solver.

2.2 Dynamic loading

When the fault reaches a critical state, where the shear stress exceeds the fault strength, the fault is reactivated and an acceleration is expected. Therefore, in this phase, the model is solved with the elastodynamic equation:

$$\mathbf{M}\ddot{\mathbf{u}} + \mathbf{C}\dot{\mathbf{u}} + \mathbf{K}\mathbf{u} = \mathbf{f}, \tag{6}$$

$$\mathbf{u}_n = \mathbf{M}^{-1}\left(\Delta t^2\left(\mathbf{f}_n - \mathbf{K}\mathbf{u}_{n-1}\right) - \Delta t\,\mathbf{C}\left(\mathbf{u}_{n-1} - \mathbf{u}_{n-2}\right)\right) + 2\mathbf{u}_{n-1} - \mathbf{u}_{n-2}, \tag{7}$$

$$\begin{aligned} \Delta \mathbf{u}_n = &\mathbf{M}^{-1}\left(\Delta t^2\left(\Delta \mathbf{f}_n - \mathbf{K}\Delta \mathbf{u}_{n-1}\right) - \Delta t\,\mathbf{C}\left(\Delta \mathbf{u}_{n-1} - \Delta \mathbf{u}_{n-2}\right)\right) + 2\Delta \mathbf{u}_{n-1} \\ &- \Delta \mathbf{u}_{n-2}. \end{aligned} \tag{8}$$

Eq. 8 gives the displacement on nodes without constraints. For the simulation of a fault failure, a constrained dynamic solution is achieved via a forward incremental Lagrange Multiplier method:

$$\lambda_n = \left(\Delta t^2 \mathbf{G}\mathbf{M}^{-1}\mathbf{G}^{\mathrm{T}}\right)^{-1}\left(\mathbf{G}\Delta \mathbf{u}_n - \mathbf{I}_n\right)\Delta \mathbf{u}_n = \Delta \mathbf{u}_n - \Delta t^2\,\mathbf{M}^{-1}\mathbf{G}^{\mathrm{T}}\lambda_n, \tag{9}$$

where the Lagrange multiplier λ_n can be interpreted as the nodal force required to satisfy the constraints on the solution $\mathbf{u}_n$.

When the governing equation switches to the elastodynamic equation, the dynamic simulation solves not only the strain and stress field, but also the dynamic slip of the fault and the seismic wave propagation problem. The dynamic simulation has a relatively short duration, in the order of seconds. Therefore, the pressure variation is considered negligible.

The (quasi-)static dynamic hybrid loading is implemented in this research to address the drawbacks and combine the advantages of both loading schemes: using the fast static solver for gradual loading and the dynamic solver for fault failure. The hybrid model is realized by updating the stress field in the dynamic simulation from the previous static solution, if the fault is unstable. At the end of each dynamic run, the slip state is evaluated, and the simulation switches back to the implicit static solver if the fault is stabilized. At the same time, the simulation updates the stress and the displacement fields from dynamic simulation for the next quasi-static iteration.

2.3 Friction, element size, and time step

For fault strength and friction calculations, we use the linear slip-weakening law as described by

$$\mu = \mu_{\mathrm{r}} + \max(0, 1 - D/D_c)\,(\mu_{\mathrm{s}} - \mu_{\mathrm{r}})\,. \tag{10}$$

`GMSH` (Geuzaine & Remacle, 2009) is used to generate the finite-element mesh for 2-D and 3-D simulations. We use a triangular, unstructured mesh to simulate the 2-D benchmark model. For that problem, the mesh size is smallest (0.6 m) at the reservoir interval near the fault, and increases to 40 m near the outside boundary of the model. For 3-D simulations, tetrahedral elements are used, with the element size ranging from 4 m at the reservoir offset interval near the main fault to 200 m near the model boundary. This results in a total of about $80,000$ elements for 2-D models and around $1,000,000$ elements for 3-D models.

In the 2-D benchmark model, we use the same linear slip-weakening friction law to evaluate the fault strength, with the initial friction coefficient $\mu_{\mathrm{s}} = 0.6$, residual friction coefficient $\mu_{\mathrm{r}} = 0.45$, and critical slip distance $D_c = 0.005\,\mathrm{m}$. According to Day et al. (2005), the resolution of the coherence length should be between 5 and 10 in order to provide an accurate simulation. Based on Uenishi and Rice (2003) and Galis et al. (2015), Wentinck (2018) derived the following coherence length for 3-D simulations in the case of slip-weakening friction:

$$\frac{L_{nuc}}{D_c} = \sqrt{\frac{3.82\pi}{4}}\frac{\mu}{\sigma_n'\,(\mu_s - \mu_r)}. \tag{11}$$

Given a shear modulus $\mu = 6\,\mathrm{GPa}$, effective normal stress $\sigma_n' = 30\,\mathrm{MPa}$, $\mu_s - \mu_r = 0.15$, and critical slip distance $D_c = 0.005\,\mathrm{m}$, the critical slip patch length $L_{nuc} = 23.1\,\mathrm{m}$. In that case, an element size of 4 m is sufficient to accurately resolve the rupture.

As mentioned in Section 2.1 with regard to quasi-static loading, by manually assigning the pressure value in the solution space, the quasi-static time step Δt is no longer present in the governing equation (3). The depletion Δp in each quasi-static step becomes the main input for the resulting displacement field $\Delta\mathbf{u}$. As the quasi-static loading is linear while the triggering of the seismic rupture is a nonlinear process, we have extended the method of Meng (2017) by introducing a modeling strategy that searches for the depletion value for triggering and reduces the effect of overshooting. After the initialization of the model with the boundary conditions, we apply an 1-MPa depletion step for each quasi-static step to search for the triggering depletion value at which the seismic event occurs. Then, the simulation using the same model setting is repeated with a 1-MPa depletion step for the previously stable quasi-static step, and then changed to a 0.1-MPa depletion step for the previously seismic step until a seismic event occurs. If necessary, for example when multiple seismic slip patches are initiated during the seismic rupture, the seismic step is further reduced to a smaller depletion step, until the seismic event exhibits only a single initial seismic slip patch.

The time for the dynamic simulation is set to $2\,\mu$s for the 3-block model and $20\,\mu$s for the model with the realistic Zeerijp reservoir geometry. `GMSH` automatically refines the unstructured mesh based on the model geometry. As the geometry of the Zeerijp model is much more complicated, `GMSH` refines the mesh further at locations with denser geometry constraints, such as at sharp and dense-line intersections. We make the time step small enough so that the explicit dynamic simulation remains stable during the simulation of the rupture.

3 Benchmark: 2-D poroelastic problem

The fault offset strongly influences the induced stress field in a uniformly depleted reservoir, as numerically shown by Van den Bogert (2018) and Buijze et al. (2019) in the

2-D case. Jansen and Meulenbroek (2022) derived an analytical expression for the poroelastic stress due to a displaced fault. The stress concentration caused by the reservoir offset strongly affects the regime of fault reactivation due to reservoir depletion. Because of the importance of stress concentration due to the reservoir offset, we at first test our results with respect to the 0- and 50-m offset models of Buijze et al. (2019).

3.1 model design

Buijze et al. (2019) simulated the stress changes and the resulting dynamic rupture caused by reservoir depletion with a 2-D poroelastic model using the finite-element code `DIANA` (DIANA, 2023), with quasi-static and dynamic hybrid loading, similar to our work. The simulation of Buijze et al. (2019) calculated the induced stress field from uniform reservoir depletion in a quasi-static scheme. When the shear stress exceeds the friction, the slip patch occurs and expands with further depletion. When the growing slip patch reaches the critical length, the seismic rupture occurs from the dynamic simulation.

We benchmark `Defmod` with the same 2-D induced seismicity problem with quasi-static loading and dynamic simulation. For the detailed model setup, we refer to Buijze et al. (2019), including material parameters, hydrostatic pressure, initial stress, and boundary conditions. Instead of the transfinite mesh, we implement the triangular mesh in our 2-D models with a mesh resolution comparable to that of Buijze et al. (2019) during the initialization of the model. In our simulations, the high resolution at the reservoir interval results in oscillations of the stress field on the fault, while such oscillations does not occur during actual reservoir depletion. Therefore, we chose to import the initial stress from Buijze et al. (2019) so that we could simulate the benchmark problem with a similar mesh size.

Note that additional differences exist in the implementation of the fault constraints despite the fact that the two codes solve both the quasi-static loading and the dynamic rupture following the same governing equations. The finite-element code `DIANA` modeled the fault with interface elements, while `Defmod` imposes fault constraints with the Lagrange Multiplier (LM) capping method without using the interface element. This difference results in different definitions of the pressure at the fault. `DIANA` directly obtains the pressure of all fault nodes from the interface elements. `Defmod` obtains the pressure of a fault node from the weighted average pressure of all elements that share the same fault node.

Both codes consider linear poroelasticity before the fault becomes critical. After the fault becomes critical, the non-linear rupture process occurs as the aseismic slip appears and expands with further depletion. Our study defines the aseismic slip as a stable shear slip of the fault. During dynamic simulation, the slip is stable and confined to the localized area without the expansion of the rupture. According to Buijze et al. (2019), the aseismic slip can transform into seismic slip if the length of the aseismic slip patch reaches a critical value before the slip patch is fully weakened. Therefore, capturing the transition from aseismic slip to seismic slip is important. Different methods are used in the two codes to capture this transition. `DIANA` implements the so-called arc-length method to adjust the depletion adaptively in order to address the nonlinear problem of dynamic rupture. As `Defmod` focuses on 3-D simulation, the computation cost for implementing such a method is prohibitively high. The convergence for the nonlinear problem becomes prominent when the aseismic slip turns into a seismic slip. Therefore, we choose to manually adjust the depletion value based on a search method discussed in section 2.3. In this way, the computation cost remains low, while the overshooting effect is reduced.

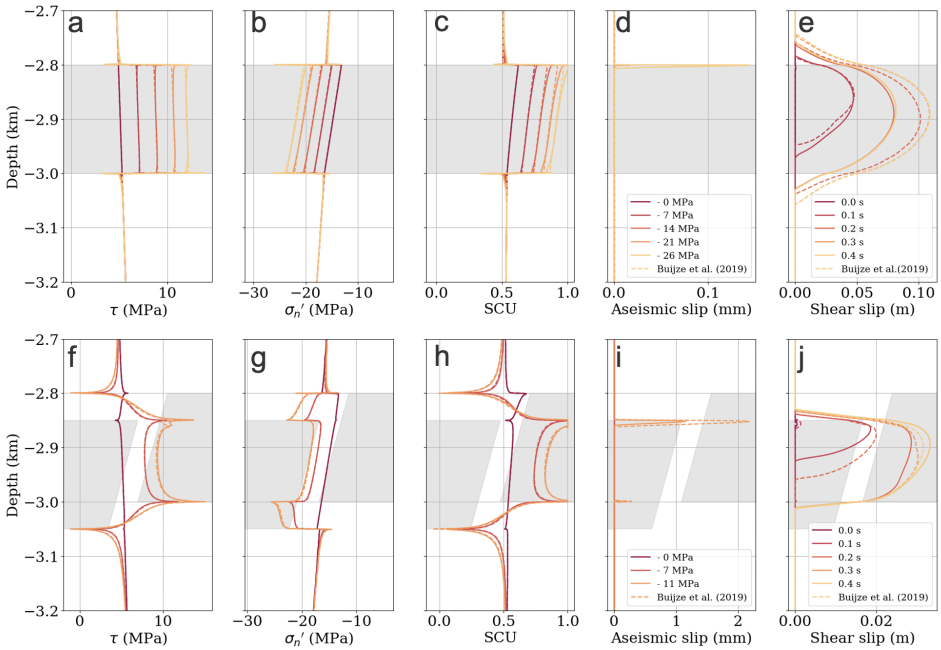

Figure 1. Benchmarking our 3-D modeling results using results from 2-D models of Buijze et al.(2019). a - e: benchmarking results for the zero-offset model. f - j: results for 50-m offset model. The solid lines show our results using `Defmod`. The dashed lines show the results of Buijze et al. (2019). The gray areas indicate the reservoir interval.

3.2 benchmark result

Fig. 1 shows the results for quasi-static loading and dynamic rupture from the benchmark test. Negative values in the normal stress indicate the compressive force. The results from two different codes share the same major features on the the incremental stress field. However, because of the different implementations of the fault constraints, differences are observed at the boundary of the reservoir. We believe that these are caused mainly by the use of the interface elements in `DIANA`.

The results show that the LM capping method for fault constraining used in `Defmod` offers results that are similar to those of the interface element method in `DIANA` for the incremental stress field. The differences mainly occur on the reservoir boundary, where the incremental pore-pressure contrast is located. The differences are caused by the fact that `Defmod` treats the pore pressure at a node as an element-wise average, whereas in `DIANA` the pore-pressure value is independent of the values in other elements. This results, in our case, in a smoother incremental pressure across the reservoir boundary, which affects the incremental stress field at the reservoir boundary. This, in turn, causes a spike for both shear stress and effective normal stress at the reservoir boundary. Consequently, the depletion value required for the seismic slip and the dynamic fault slip is lower in the case of our simulation using `Defmod`. This effect is most prominent for the zero-offset benchmark model.

The depletion values corresponding to triggering of the seismic slip for the model with zero-offset are different between the two approaches: with `DIANA` it is 30.17 MPa, with `Defmod` the value is 26 MPa. This difference is mainly due to the different methods for fault implementation. For the 50-m offset benchmark model, the triggering depletion values are more similar: 10.76 MPa for `DIANA` and 11 MPa for `Defmod`. In this

case, the effect of the incremental stress field caused by the fault offset is more prominent than the effect of the fault-implementation method. For the zero-offset model, the lower triggering depletion value in `Defmod` results in a lower value of the shear capacity utilization (SCU) in the reservoir interval outside the aseismic slip patch when the seismic nucleation occurs. This causes lower amplitude and a shorter length for the slip patch, despite the similarity in the onset of the rupture before 0.1 s. However, for the 50-m offset model, the similar triggering depletion values result in similar rupture length and slip amplitude. In this case, however, because `DIANA` implements a Newton solver and adaptively changes the depletion step until the seismic slip occurs, the result has a more substantial slip-weakening effect from the aseismic slip patch when the seismic slip occurs, compared to the result of `Defmod`. As a result, `Defmod` produces a faster acceleration and a slightly larger slip at the reservoir juxtaposition for a higher shear stress at the rupture patch. In general, `Defmod` offers comparable results to `DIANA`, capturing the same main features of induced seismicity.

4 3-block reservoir model

To better understand the effects of the 3-D geometry of the source region on the occurrence of induced earthquakes, we have developed a set of models. These models focus on a number of prominent features of the source region that can strongly influence the generation of Zeerijp earthquake, induced by reservoir depletion. The fault-zone geometrical features include the varying offset, the intersection angle of the normal faults, and the shape of the resulting reservoir compartments. With the 3-block models, we investigate these geometrical features on the induced stress field, the fault reactivation, and the fault evolution.

4.1 3-block model design

In the geological model by NAM (2020), shown in Fig. 2d, the reservoir is split by the fault system into multiple compartments. According to Wentinck (2018), the hypocenter is located at the main fault (mFS7-Fault-54) and near the conjunction with the secondary fault (mFS7-Fault-53). The effects of an offset reservoir have been extensively studied. However, complicated offset patterns with, for example, the horst formed here by two intersecting normal faults, were rarely discussed. To investigate the relationship between reservoir geometry (horst) and induced seismicity, we created a simplified 3-block model focusing on the horst shape formed by the two intersecting faults. Furthermore, by varying the intersection angle, we changed the shape of the horst and compared the induced stress field and the resulting seismic ruptures. To focus on the effect of the reservoir geometry, we decided to reduce the complexity of the model by including a similar composition (overburden, reservoir and underfunded) to the benchmark model discussed above.

In the 3-block models, we included a secondary fault, intersecting the main fault at the center, forming the reservoir compartments. The secondary fault is a vertical planar fault with a dip of 90° and an azimuth based on the intersection angle with the main fault: 90°, 60°, or 30°. The main fault has a 66° dip and cuts through the entire model, while the secondary fault ends at the intersection with the main fault. Note that we assume that the secondary fault remains stable during the entire simulation.

The reservoir is first split (offset) by the main fault, and then by the secondary fault. This results in a 3-compartment setup, shown in Fig. 2. The intersection angle controls the shape of the horst structure. These 3-block models with varying offsets on the main fault represent possible variations in the Zeerijp reservoir geometry. Such a structure also prevents the entire main fault from slipping due to a uniform depletion of the reservoir. The fault offset on the reservoir across the main fault changes from 0 to 100 m, from the x-boundary to the center of the model. The faults intersect at the center of the model,

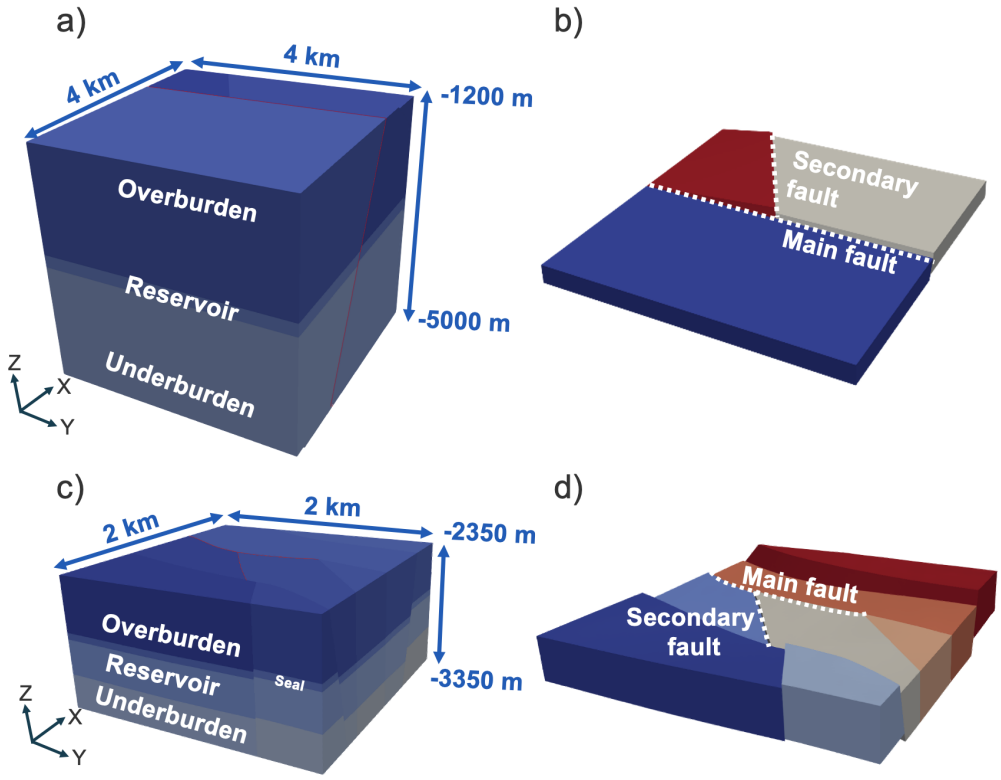

Figure 2. Geometry for the 3-D models. The 3-block models with a 60° intersection angle between the two faults (a) and its reservoir geometry (b). The source region geometry (c) of the Zeerijp model and its reservoir geometry (d) from the NAM (2020) database.

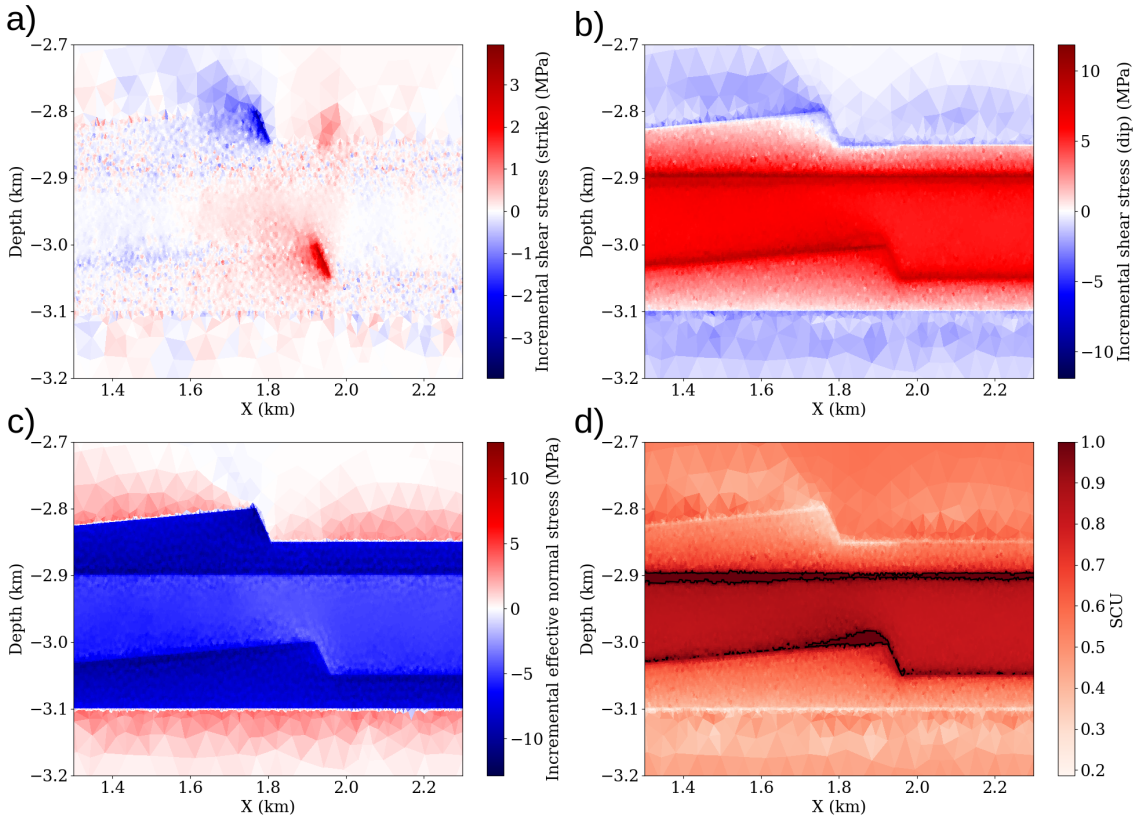

Figure 3. Incremental shear stress in strike direction (a) and in dip direction (b), incremental effective normal stress (c), and SCU (d) after a 12.5 MPa uniform depletion of the reservoir for the 3-block model with a 30° intersection angle between the two faults.

and then the offset drops by 50 m across the intersection line. The reservoir has a constant offset of 50 m across the secondary fault.

The 3-D models have the same material properties as the benchmark model (Buijze et al., 2019). However, unlike those simulations, we do not impose any initial stress at the fault in our modeling, but initialize the model with gravity and gravity-based boundary traction. The boundary traction on both x- and y-boundaries are compressive. The ratio of the boundary traction to maximum vertical stress is 0.748 and 0.795 in, respectively, the x- and y-direction. In this setting, the maximum horizontal stress is aligned with the strike of the main fault, and the minimum horizontal stress is aligned with the dip azimuth. After the initialization of the model, we apply roller boundary conditions at the side walls to simulate a laterally extended reservoir. Then we apply the adaptive stepping method mentioned in section 2.3 to simulate the resulting seismic rupture. The 3-block models incorporate the same friction parameters as the 2-D benchmark model.

4.2 3-block model simulation results

The simulations for the three different 3-block models clearly show the effect of the angle of intersection between two faults on the induced stress field, assuming uniform reservoir depletion. Fig. 3 shows the incremental stress field on the main fault, with a 30° intersection angle between two faults, after a 12.5 MPa uniform depletion of the reservoir. Note the relatively strong incremental shear stress in the strike direction. This is

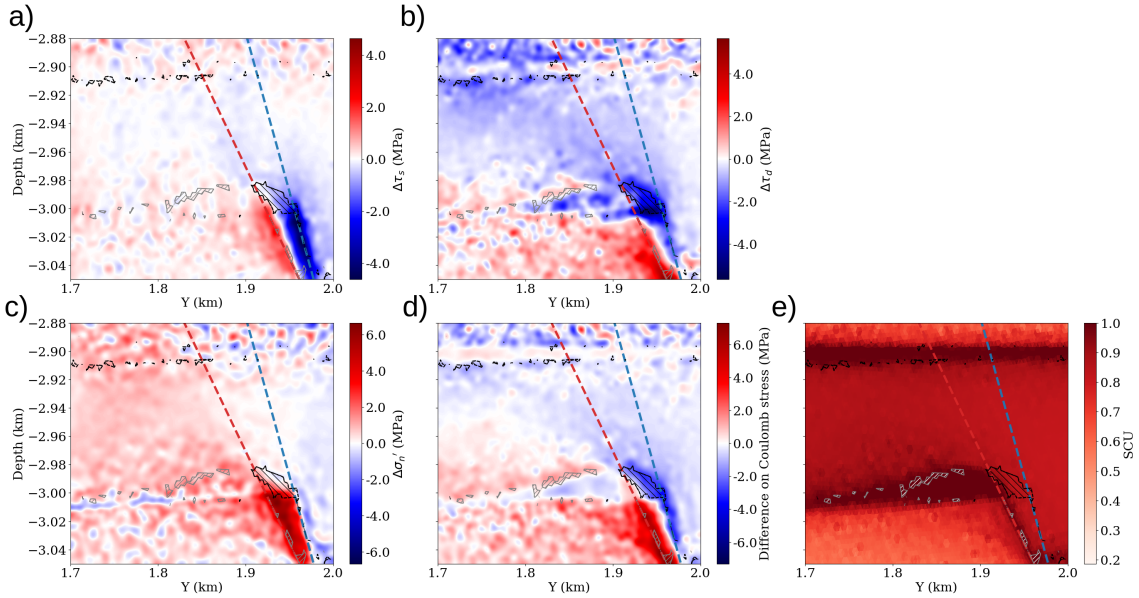

Figure 4. (a–d) Difference of induced stress fields at a 12.5 MPa depletion between the models with a 30° and 45° intersection angle between the faults. (e) The SCU values corresponding to the occurrence of seismic events for the model with a 30° fault intersection. The gray dashed area indicates the additional critical area for the model with a 45° fault intersection, and the black dashed area the reduced critical area.

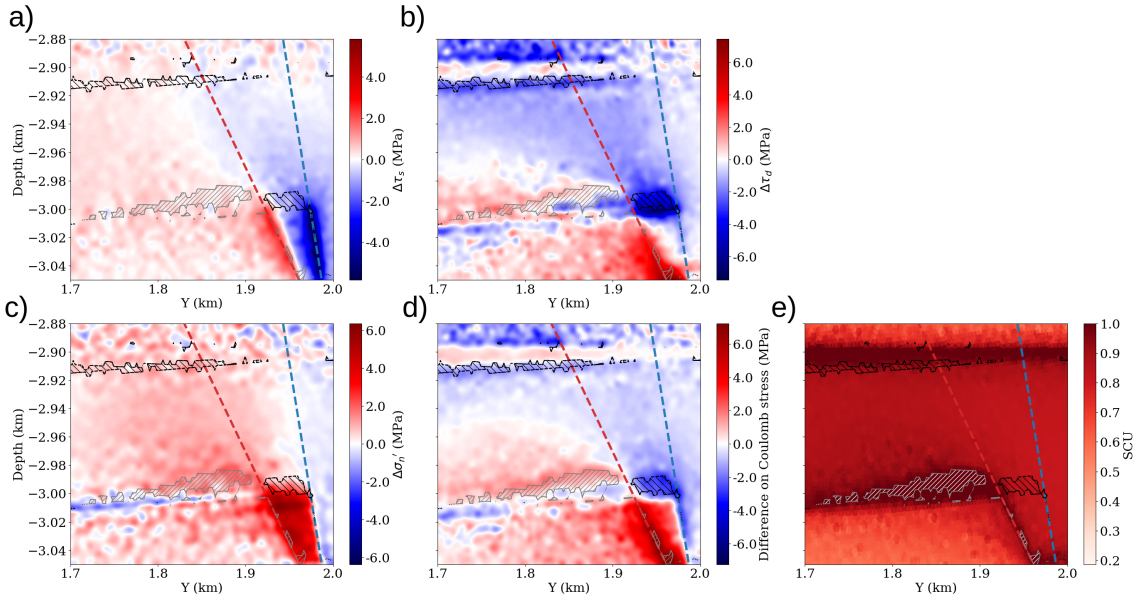

Figure 5. (a–d) Difference of induced stress fields at a 12.5 MPa depletion for the models with a 30° and 60° intersection angle between the faults. (e) The SCU values at the seismic events for the model with 30° fault intersection. The gray dashed area indicates the additional critical area from the model with a 60° fault intersection, and the black dashed area the reduced critical area.

caused by the topography of the compartments located at the reservoir boundary next to the intersection line. This happens because the reservoir compaction has a horizontal component from the 3-step reservoir compartmentalization as a result of varying offsets of both the main fault and the secondary fault.

The reservoir offset on the main fault causes a concentration of incremental stress from a uniformly depleted reservoir, as was also observed in the previous studies on the induced stress field of a displaced fault (Van den Bogert, 2018; Buijze et al., 2019; Candela et al., 2019; Jansen & Meulenbroek, 2022). Fig. 3 illustrates the stress concentration at the juxtaposition boundary for shear stress in the dip direction and the effective normal stress, resulting in high SCU values at the same location. Importantly, the 3-block models have a varying fault-offset on the reservoir, where the offset changes from 0 m from one boundary to 100 m at the intersection, then drops to 50 m across the intersection line till the other boundary. The highest SCU value on the main fault is located near the area with the largest offset value. This area is close to the intersection line at both top and bottom of the reservoir juxtaposition interval. The location at the intersection line has the largest offset, but the SCU is not the highest there. The highest SCU occurs at a location with a slightly smaller offset. This is because the offset rapidly drops from 100-m to 50-m across the intersection, leading to a lower SCU value in the region of the largest offsets.

The SCU data in Fig. 3 show that the main fault at top and bottom of the reservoir juxtaposition becomes critical when SCU = 1. However, the slip patches remain aseismic until the length of the patch reaches a critical value measured in the direction of the maximum shear stress, according to Uenishi and Rice (2003) and Buijze et al. (2019). However, due to the complicated structure of the fault offset, an analytical computation of such a critical length for the transition from aseismic to seismic slip is not possible.

Given the same boundary condition and the same depletion pattern, the triggering depletion values for the seismic event are similar in the three 3-block models. The value of reservoir depletion required to trigger a seismic event for models with a 30°, 45°, or 60° intersection angle between the faults are 12.5 MPa, 12.6 MPa, and 12.6 MPa, respectively. Fig. 6 illustrates the result of our dynamic simulation of the seismic event for the three models. Our results indicate a change in the rupture pattern with different intersection angles. This includes important changes in the initial slip patch and in the rupture evolution.

For the 3-block model with a 60° fault intersection angle, the dynamic simulation shows that an initial seismic slip patch occurs at the top of the reservoir juxtaposition interval close to the intersection line. We refer to this location on the fault as slip patch A, as marked in Fig. 6c. This initial slip patch expands in both dip and strike directions. The expansion in the dip direction stops at the boundary of the reservoir juxtaposition. In contrast, the expansion in the strike direction propagates from the initial slip patch to the whole reservoir juxtaposition. The location of the maximum slip shares its location with that of the initial slip patch.

The dynamic simulation for the 3-block model with a 30° intersection angle exhibits an initial slip patch at the bottom of the reservoir juxtaposition interval close to the intersection line. This we will refer to as slip patch B, shown in Fig. 6. Unlike slip patch A (60° fault intersection model), the slip patch B expands from the bottom to the top of the reservoir juxtaposition. The initial slip patch B expands in both the dip and strike directions, and then propagate within the whole reservoir juxtaposition. In this model, the maximum slip location is located at the bottom of the reservoir juxtaposition, the same as the location of the initial slip patch.

The dynamic simulation result for the 3-block model with the 45° intersection shows an intermediate pattern, compared to the earlier two models. The initial slip patch shares

the same location as slip patch B, while the maximum slip is located in between the slip patches A and B, instead of at either of them.

All the seismic ruptures in the 3-block models propagate through the whole reservoir juxtaposition. The rupture not only propagates in the dip direction but also along the strike direction within the juxtaposition. The propagation in the strike direction can be explained by the fact that the 3-block models are the lateral extensions of the 2-D model, as the models have limited heterogeneity in the strike direction except for the varying offset. Furthermore, the triggering depletion for the 3-block model is similar to that of the 2-D offset model.

The difference in the initial slip patch for the 3 models with different intersection angles can be explained by their respective incremental stress field. Fig. 5 shows the difference in the incremental stress field between the 30° and 60° intersections at 12.5 MPa depletion. Note that the different fault intersection angle results in distinctive fault and reservoir compartment locations, thus affecting the distribution of pressure depletion on the main fault.

Fig. 5 shows that, after 12.5 MPa depletion, compared to the 60° fault intersection, the 30° fault intersection produces a larger incremental stress in the dip direction and a smaller effective normal stress at the lower reservoir juxtaposition. This difference corresponds to the area of the slip patch B during the seismic event. The incremental shear stress in the strike direction is not much affected by the location of the fault intersection. Fig. 5d shows the Coulomb stress difference between the two cases. The lower half of the reservoir juxtaposition has a positive value, indicating the promotion of slip in the area. The maximum value is observed at the fault intersection. However, this is due to the change in the location of the secondary fault.

Fig. 5e shows the SCU value corresponding to the occurrence of the seismic events, at 12.5 MPa depletion for the 30° intersection and 12.6 MPa depletion for the 60° intersection. Here, $SCU = 1$ indicates a critical state: the area turns into either a seismic slip patch or an aseismic slip patch. The contoured area denotes an increase and decrease in size of the slip patch compared with the 60° fault intersection. Fig. 4e shows the SCU value and the difference in slip patch between the models with a 30° and 45° intersection angle, corresponding to the occurrence of the seismic events. We see an intermediate difference with respect to the previous comparison, where the size of the increased and decreased slip patches are smaller than that for the model with 45° fault intersection.

In general, our results illustrate that a smaller intersection angle between the two faults promotes the slip patch to form at the lower reservoir juxtaposition, and is more likely to initiate a seismic slip at the location of slip patch B. The maximum slip location shows the same trend in all cases.

5 Zeerijp model

5.1 Zeerijp model design

To verify our findings from the 3-block models pertaining to the relationship between the fault intersection angle and the rupture patterns, we construct a $2\times2\times1\,\mathrm{km}^3$ model focusing on the Zeerijp region in Groningen, the Netherlands. For this purpose, we make use of the Petrel geological model of the Groningen gas field (NAM, 2020). This geological model was created from stratigraphic and structural information derived from well-log and seismic data. We reconstruct the fault planes and the horizons using the point cloud data from this realistic geological model. The smoothly reconstructed fault planes and horizons are used to construct the mesh with `GMSH` for our 3-D finite-element simulation.

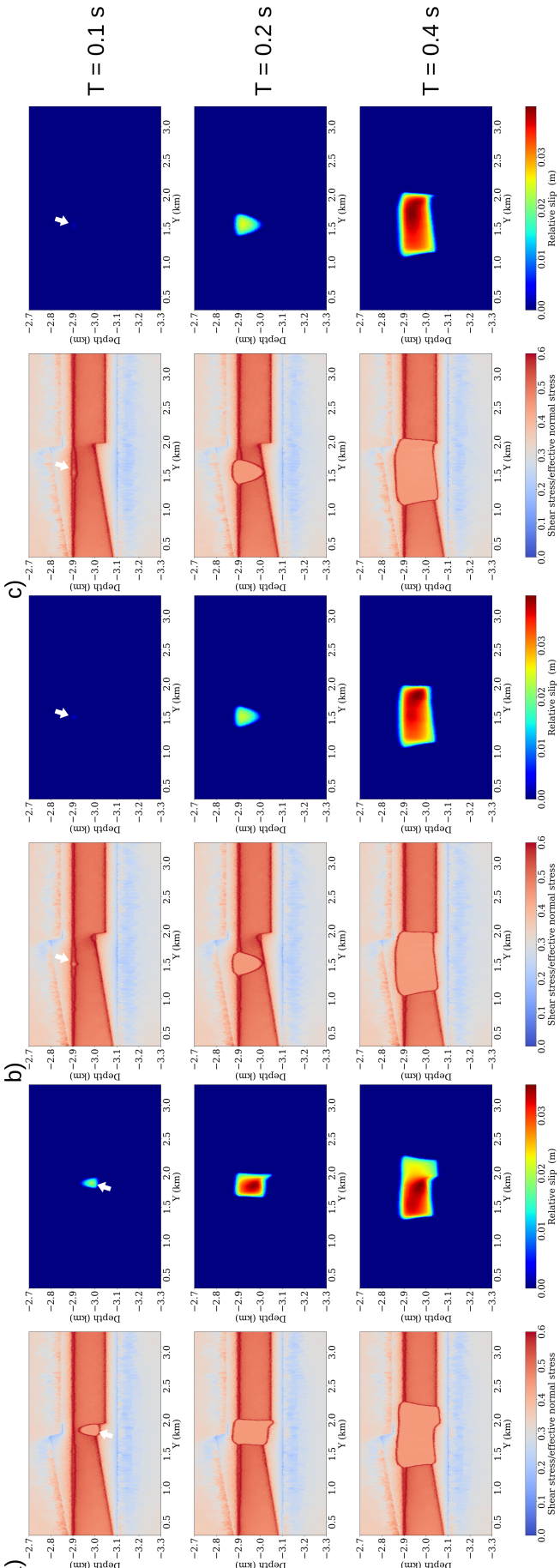

Figure 6. Results of the dynamic simulation for each of the 3-block models, showing the temporal evolution of stress and induced slip. The arrow indicates the location of the initial slip patch. a) The seismic event at 12.5 MPa reservoir depletion for the model with 30° intersection angle between the two faults. b) The seismic event at 12.6 MPa reservoir depletion for the model with 45°-degree intersection. c) The seismic event at 12.6 MPa reservoir depletion for the model with 60°-degree intersection.

Formation	depth of the top (m)	density (kg/m3)	Poisson ratio (-)	Young's modulus (static) (GPa)
Zechstein	1200	2150	0.29	23.7
Anhydrite	∼2800	2840	0.26	45.3
Rotliegend sandstone	∼2850	2430	0.20	15.0
Carboniferous underburden	∼3150	2650	0.27	18.4

Table 1. Material properties of the Zeerijp model, from Wentinck (2018).

According to the Petrel model, the research area contains multiple formations within the reservoir interval. To focus on the effect of the 3-D reservoir geometry, we choose to include only the Zechstein overburden, the anhydrite top seal, the Rotliegend reservoir, and the Carboniferous underburden (basement). All the formations are considered to be homogeneous within the layers. The elastic modulus for these four formations were taken from Wentinck (2018), who calculated these moduli using seismic P-and S-wave velocities. Here we also use the same relation between the static and dynamic Young's modulus, namely, $E_{dyn} = 2 \times E_{sta}$. The material is considered to be homogeneous inside each formation. The model includes all major faults within the area of interest, together with appropriate fault offsets on the reservoir and the top seal. These fault offsets result in several reservoir compartments that control the topography of the reservoir.

In this study, fault constraints are implemented only on the main fault mFS7-Fault-54, near the hypocenter of the 2018 Zeerijp M_L 3.4 earthquake as derived from seismic moment tensor inversion (Dost et al., 2020). The other faults that are present in the model are considered stable and are characterized by their offsets on the reservoir, but their stress states are not distinguished. In our simulation, only the main fault is allowed to slip. The effect of fault intersections are examined in terms of their geometry. Dynamic triggering from one fault to another is not possible in this case.

The same boundary conditions as for the 3-block models discussed earlier have been considered for this model. The model is initialized with gravity and gravity-based boundary traction. After the initialization, uniform depletion is applied to the reservoir in order to simulate the induced stress field due to reservoir depletion until the first seismic slip occurs on the main fault. The friction parameters that we consider for the 3-D Zeerijp model are different from those for the 3-block models. The initial friction coefficient $\mu_{\mathrm{s}} = 0.4$, residual friction coefficient $\mu_{\mathrm{r}} = 0.3$, and critical slip distance $D_c = 0.2\,\mathrm{m}$. These friction parameters constitute representative values.

5.2 Zeerijp model simulation results

To investigate how the incremental stress field and the fault rupture develop in case of a realistic, relatively complex reservoir geometry as the Zeerijp Petrel model, we perform our simulations. The reservoir geometry of the Zeerijp region is shown in Fig. 2. The incremental stress field at the main fault after a 16 MPa depletion of the reservoir is illustrated in Fig. 7. The stress field exhibits an offset-controlled stress pattern. The intersection between the main and the secondary faults in the Zeerijp model is 44.5°. With the fault offset having a pattern similar to the 3-block models (see Section 4), the location of the reservoir offset for the secondary fault exhibits a large incremental shear

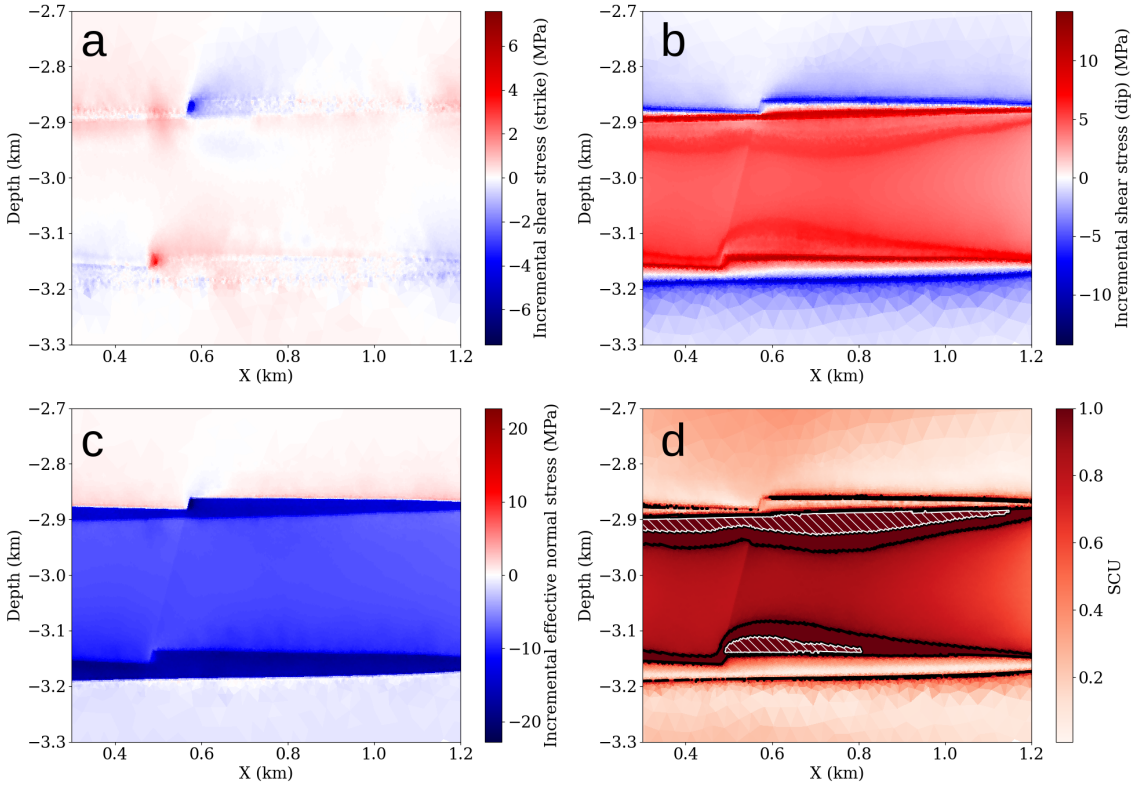

Figure 7. Incremental stress field for the Zeerijp model after a 26 MPa depletion. The black lines in (d) contour the critical area with SCU=1, and the white dashed areas represent critical areas that are fully weakened.

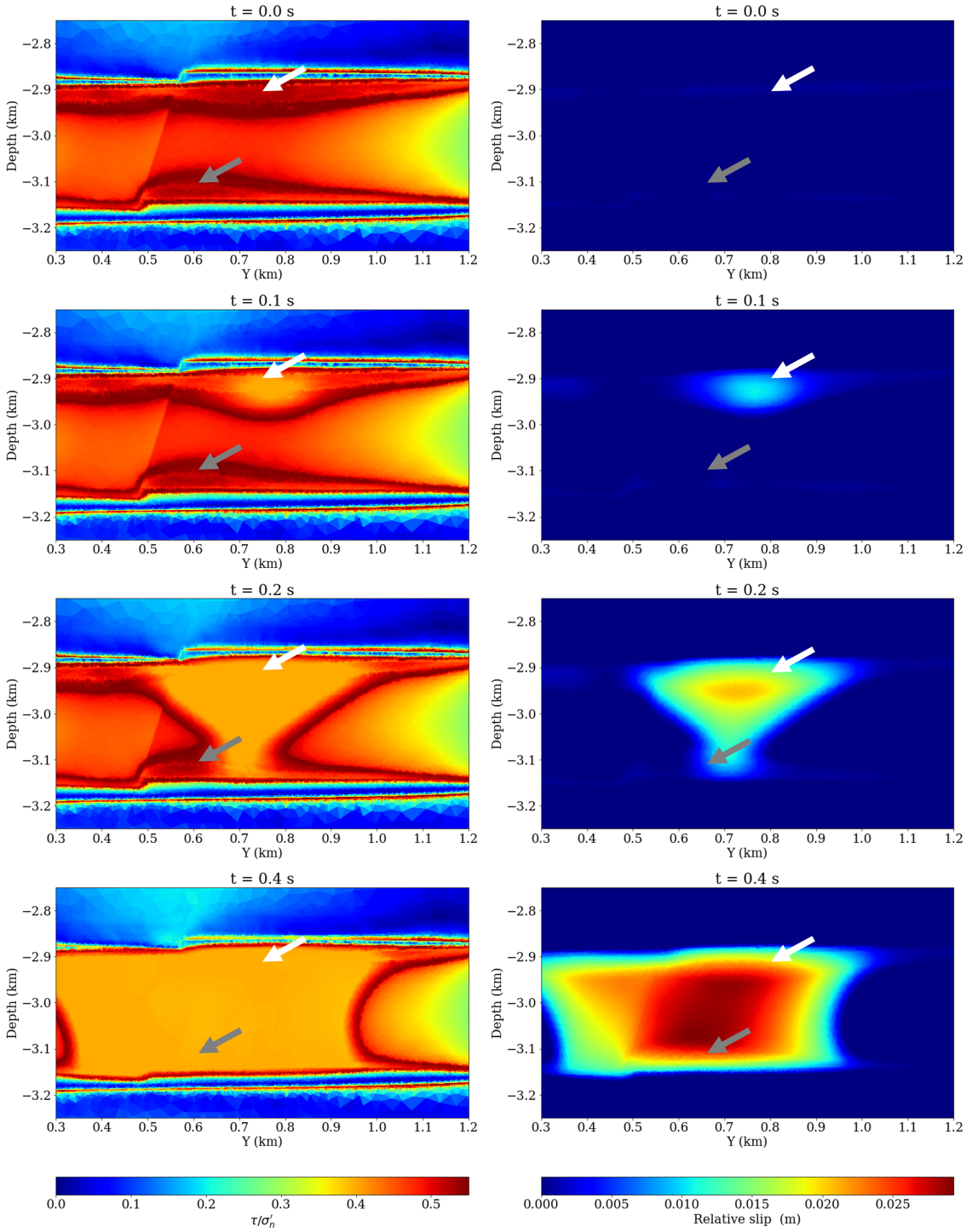

Figure 8. Dynamic simulation of the seismic event at a 26 MPa reservoir depletion for the Zeerijp model with a 30° intersection angle between the two faults. The white arrow indicates the location of the original seismic slip patch. The gray arrow indicates the location of the original aseismic slip patch. The pictures on the left show the ratio between shear stress and effective normal stress τ/σ_n' and on the right the relative slip.

stress in the strike direction, with opposite directions at the top and at the bottom of the reservoir juxtaposition near the intersection. At the same location, the incremental effective normal stress is relatively weak at the bottom and strong at the top. The SCU values also show critically stressed slip patches both at A and B.

The reservoir compaction due to the distribution of reservoir compartments has a similar effect as that of the simplified models. This prevents the top of the reservoir juxtaposition at the intersection line from slipping, but promotes slipping at the bottom. This effect, together with the transition of the offset at the intersection, moves the location of the initial slip patch slightly away from the intersection line having the largest reservoir offset, as shown in Fig. 8.

A 50-m thick basal anhydrite layer is placed on top of the reservoir to better represent the geological structure of the gas reservoir at Zeerijp. The presence of this anhydrite layer increases the Coulomb stress on the main fault at the location of the top seal, and decreases the Coulomb stress on top of the top seal. The top seal hardly affects the incremental Coulomb stress within the reservoir interval.

From the modeled distribution of stress, we can clearly identify two major slip patches on the fault plane after a 26 MPa uniform depletion of the reservoir. These two slip patches resemble also to the slip patches found for the 3-block models discussed earlier. The seismic slip patch occurs at the top of the reservoir juxtaposition near the intersection, corresponding to the location of slip patch A in the 3-block model. The aseismic slip patches are located at the boundary of the reservoir juxtaposition. At the bottom of the reservoir juxtaposition, there is a major aseismic slip patch corresponding to the location of slip patch B in the 3-block model.

These slip patches remain aseismic until one patch reaches its critical length or is merged with a seismic slip patch. At the same time, the slip patch continues to be weakened with further depletion of the reservoir. Fully weakened fault nodes in the slip patch before the slip patch reaches its critical length decrease the length of slip patch, as the patches cannot be further weakened during fault reactivation.

Fig. 8 shows the result of dynamic simulation of the seismic event for the Zeerijp model. The seismic slip initiates at slip patch A. The initial slip patch expands and merges with the aseismic slip patch B. After the merging, the slip patch further expands in the strike direction, while the expansion in the dip direction gets halted at the reservoir juxtaposition. The area between the two slip patches has the maximum slip during dynamic simulation.

However, unlike the 3-block models, for the Zeerijp model the weakening is observed at both slip patches due to reservoir depletion—till the onset of the seismic event. This difference between the two models can be related to the model geometry and boundary conditions. Within slip patches A and B, a fully-weakened patch expands from the boundary of the reservoir juxtaposition to the center of the juxtaposition. According to the results of 2-D simulation by Buijze et al. (2019), one of the conditions for the occurrence of seismic slip is that the slip patch cannot be fully weakened before the critical length for the seismic slip is reached. However, the situation becomes significantly more complicated in case of 3-D simulations considering more realistic structural complexities. Our results of dynamic simulation using relatively complex 3-D models show that the fully-weakened slip patches are always located within the expanding slip patches. Although the fully-weakened slip patches are not susceptible to further weakening, their SCU values are still equal to 1. This SCU value allows the rupture front to propagate through. Therefore, in this case, the slip patch length is measured in the dip direction, and is then subtracted from the length of the fully-weakened slip patch. In our case, due to the steep dip angle of the main fault, we measure the slip patch length based on its depth interval. The analytical rupture length for the seismic event is 72.2 m when the dynamic Young's

modulus $E_{dyn} = 2 \times E_{sta}$, and 36.1 m when the static Young's modulus is estimated from equation 11. The simulated slip patch length corresponding to the occurrence of the nucleation is 77.3 m, and 33.3 m if the fully weakened area is excluded.

The magnitude of the seismic event calculated from the slip data of our 3-D simulated seismic rupture is $M_W = 3.0$. This value matches well with the magnitude $M_L = 3.4$ obtained by inversion of observed seismological data for the Zeerijp earthquake (Dost et al., 2020). The assumption that the dynamic Young's modulus is twice the quasi-static Young's modulus is same for both these magnitude estimations. From our simulation, the depletion value at fault reactivation is 26 MPa, identical to the triggering depletion value from Wentinck (2018), calculated using the modeled depletion rate at the ZRP-3 well location. The initial slip patch and maximum slip are close to the inverted hypocenter location, and the earthquake magnitude resembles the actual Zeerijp earthquake of 2018, according to Dost et al. (2020).

6 Concluding remarks

We have performed quasi-static and dynamic simulations of induced seismicity considering realistic 3-D reservoir structure of the Groningen gas field. The simulation results from representative 3-block models show that the line and the angle of the intersection between two normal faults have important additional effects on the induced stress field, compared with a single-fault scenario that is often considered. Our findings allow us to draw the following conclusions:

1. The results show the incremental shear stress in the strike direction of the main fault compared, which is generated due to the horizontal component of the reservoir compaction from the horst structure.
2. A smaller intersection angle increases the incremental shear stress in the dip direction at a lower reservoir juxtaposition. It also slightly decreases the incremental effective normal stress on the main fault adjacent to the horst block. The incremental Coulomb stress is increased at the lower half of the reservoir juxtaposition at the horst block.
3. Consequently, when the intersection angle between the main fault and the secondary fault changes from 60° to 30°, the location of the initial slip patch changes from the top of the reservoir juxtaposition near the intersection line to the bottom. The location of the area corresponding to the maximum slip is the same as that of the initial slip patch. For an intersection angle of 45°, we observe a transition for the location the maximum slip to be in between the location of the initial slips for the models with 30° and 60° intersection angles.
4. The triggering depletion value and the maximum slip are less affected by the fault intersection angle, despite the difference on the growth of the two major slip patches.

A realistic, 3-D model for the Zeerijp reservoir structure presents an incremental stress field which is similar to that for a representative 3-block model. The maximum slip for the seismic event is located in between the two slip patches, similar to a representative model with a 45° fault intersection angle. Our 3-D, realistic simulation produces an earthquake magnitude of M_W 3.0, due to fault reactivation occurring at a reservoir depletion value of 26 MPa. These values are similar to those for the 2018 Zeerijp earthquake of M_L 3.4 (Wentinck, 2018). The location of the simulated rupture is also close to the inverted hypocenter location for the 2018 earthquake (Dost et al., 2020).

From our results, we conclude that the reservoir geometry significantly influences the occurrence of induced earthquakes by affecting the incremental stress field, the nucleation location, the rupture pattern, and the location of the maximum slip. In the end, it plays an important role in determining the location of the hypocenter, the magnitude, and the depletion value corresponding to seismic for a depletion-induced seismic event.

We also observe the same effects for different initial stress setups, particularly for the orientation of the horizontal stresses. In one setup, we interchange the maximum and the minimum horizontal stresses in the 3-block models during the initialisation: the minimum horizontal stress aligns with the strike of the main fault and the maximum horizontal stress aligns with the azimuth of the fault dip. In the simulated result, we observe the same effects as described above on the incremental stresses, on the growth of the initial slip patch, and on the rupture pattern. However, in this setup the triggering depletion value becomes more sensitive to the intersection angle. For the models with 30°, 45°, and 60° intersection angle, the triggering depletion value is 18.8 MPa, 19.25 MPa, and 19.4 MPa, respectively. Unlike the previous setup, the rupture is arrested at 1 km from the initial slip patch in the strike direction instead of propagating through the whole juxtaposition.

Most subsurface reservoirs, like the Groningen gas field, contain fault systems where multiple faults cut the reservoir at various intersection angles and offsets. The resulting reservoir topography and the induced stress field due to reservoir depletion are more complex than those in case of a single fault, even under the assumption of uniform reservoir depletion. An incorrectly estimated stress field will lead to, for instance, a wrong estimate of the triggering depletion value and the maximum magnitude of a possible seismic event due to production activity. Consideration of realistic reservoir geometry is, therefore, of utmost importance during geomechanical simulation of reservoir-induced seismicity.

In this study, we have assumed that the secondary fault at the intersection with the main fault remains stable during the simulation. This assumption might cause underestimation of the event magnitude, as the induced shear stress in the reservoir is predominantly in the dip direction. This might result in rupture propagation from one fault to another through the fault intersection. In general, models that do not consider fault interaction can still produce reasonable simulation results, as the depletion mainly controls the incremental stress.

7 Data Availability Statement

The open-source finite-element code Defmod (Meng, 2017) was used for geomechanical simulations. The realistic reservoir geometry was constructed using the data from NAM (2020). `GMSH` (Geuzaine & Remacle, 2009) was used to generate finite-element mesh for simulation. Buijze et al. (2019) provided the 2-D benchmark results. The code and data used for generating the results present in this research are preserved at `https://doi.org/10.4121/d2e0953c-3ac6-4547-9fb4-8ceaa0ede4d7`.

Acknowledgments

This research was funded in part by NWO Science domain (NWO-ENW), project **DEEP.NL.2018.048**. We thank Chunfang Meng for providing technical support on Defmod and the benchmark problem. We are indebted to Loes Buijze for the 2-D benchmark data and her advice.

References

Buijze, L., Van den Bogert, P., Wassing, B., & Orlic, B. (2019). Nucleation and arrest of dynamic rupture induced by reservoir depletion. *Journal of Geophysical Research: Solid Earth*, *124*(4), 3620–3645.

Candela, T., Osinga, S., Ampuero, J.-P., Wassing, B., Pluymaekers, M., Fokker, P. A., ... Muntendam-Bos, A. G. (2019). Depletion-induced seismicity at the Groningen gas field: Coulomb rate-and-state models including differential compaction effect. *Journal of Geophysical Research: Solid Earth*, *124*(7),

7081–7104.

Day, S. M., Dalguer, L. A., Lapusta, N., & Liu, Y. (2005). Comparison of finite difference and boundary integral solutions to three-dimensional spontaneous rupture. *Journal of Geophysical Research: Solid Earth*, *110*(B12).

DeDontney, N., & Lele, S. (2018). Impact of production fluctuations on Groningen seismicity-geomechanical modelling using rate and state friction. *Assen: Nederlandse Aardolie Maatschappij BV*.

DIANA. (2023). *DIANA 10.7 User Manual* [manual]. Retrieved from `https://dianafea.com/diana-manuals/`. DIANA FEA BV.

Dost, B., van Stiphout, A., Kühn, D., Kortekaas, M., RuiGrok, E., & Heimann, S. (2020). Probabilistic moment tensor inversion for hydrocarbon-induced seismicity in the Groningen gas field, the Netherlands, part 2: Application. *Bulletin of the Seismological Society of America*, *110*(5), 2112–2123.

Galis, M., Pelties, C., Kristek, J., Moczo, P., Ampuero, J.-P., & Mai, P. M. (2015). On the initiation of sustained slip-weakening ruptures by localized stresses. *Geophysical Journal International*, *200*(2), 890–909.

Geuzaine, C., & Remacle, J.-F. (2009). Gmsh: A 3-D finite element mesh generator with built-in pre-and post-processing facilities. *International journal for numerical methods in engineering*, *79*(11), 1309–1331.

Hunfeld, L., Niemeijer, A., & Spiers, C. (2017). Frictional properties of simulated fault gouges from the seismogenic Groningen gas field under in situ P–T-chemical conditions. *Journal of Geophysical Research: Solid Earth*, *122*(11), 8969–8989.

Jansen, J.-D., & Meulenbroek, B. (2022). Induced aseismic slip and the onset of seismicity in displaced faults. *Netherlands Journal of Geosciences*, *101*.

Kühn, D., Hainzl, S., Dahm, T., Richter, G., & Rodriguez, I. V. (2022). A review of source models to further the understanding of the seismicity of the Groningen field. *Netherlands Journal of Geosciences*, *101*.

Maerten, L., Willemse, E. J., Pollard, D. D., & Rawnsley, K. (1999). Slip distributions on intersecting normal faults. *Journal of Structural Geology*, *21*(3), 259–272.

Meng, C. (2017). Benchmarking Defmod, an open source FEM code for modeling episodic fault rupture. *Computers & Geosciences*, *100*, 10–26.

NAM. (2020). *Petrel geological model of the Groningen gas field, the Netherlands* [dataset]. Yoda. Retrieved from `https://public.yoda.uu.nl/geo/UU01/1QH0MW.html` doi: 10.24416/UU01-1QH0MW

Uenishi, K., & Rice, J. R. (2003). Universal nucleation length for slip-weakening rupture instability under nonuniform fault loading. *Journal of Geophysical Research: Solid Earth*, *108*(B1).

Van den Bogert, P. (2018). Depletion-induced fault slip and seismic rupture-2d geomechanical models for the Groningen field, The Netherlands. *Assen: Nederlandse Aardolie Maatschappij BV*.

Van Wees, J.-D., Fokker, P. A., Van Thienen-Visser, K., Wassing, B. B., Osinga, S., Orlic, B., ... Pluymaekers, M. (2017). Geomechanical models for induced seismicity in the Netherlands: Inferences from simplified analytical, finite element and rupture model approaches. *Netherlands Journal of Geosciences*, *96*(5), s183–s202.

Wentinck, H. (2018). Dynamic modelling of large tremors in the Groningen field using extended seismic sources. *Assen: Nederlandse Aardolie Maatschappij BV*.